

Warm Molecular Gas in Hot Dust-Obscured Galaxies

Ioakeim-Gerasimos Bourbah

Heraklion, 2023



University of Crete
Department of Physics

Supervisor: Tanio Diaz-Santos

Acknowledgments

My most profound appreciation goes to my supervisor, Dr. Tanio Diaz-Santos, for guiding me through my first research project and teaching me everything I needed to know in this field. His instructions were essential in the completion of this thesis. I would also like to extend many thanks to the esteemed faculty and staff of the university for helping me achieve my career goals. Finally, I would like to express my gratitude to my family and friends for supporting me through this academic journey.

Contents

Acknowledgments	2
1 Summary	4
2 Introduction	5
2.1 Radio Astronomy	5
2.1.1 Historical Background	5
2.1.2 Radio Telescopes	5
2.1.3 Radio Interferometry	7
2.2 AGNs and Quasars	8
2.2.1 Quasars	8
2.2.2 Hot DOGs	10
2.3 Interstellar Medium	11
2.3.1 Molecular Gas	11
2.3.2 Spectral Lines	11
2.3.3 Carbon Monoxide	12
3 Data Reduction and Analysis	13
3.1 Raw Data to Dirty Image	13
3.2 Cleaning	15
3.3 Data Analysis	15
4 Conclusions	20
References	21

1 Summary

The main goal of this thesis is to estimate of the luminosity of the CO(J=7-6) line and to calculate molecular gas mass of the Hot Dust-Obscured Galaxy (Hot DOG) WISE J224607.57-052635.0 (W2246-0526 hereafter). Hot DOGs are an uncommon population of hyper-luminous, substantially dust-obscured quasars detected by the NASA's *Wide-field Infrared Survey Explorer* (WISE) mission. Observations from Atacama Large Millimeter/Submillimeter Array (ALMA) Observatory were used. The Common Astronomy Software Applications (CASA) software was used to produce the data cube of the emission line from the ALMA interferometric observations. Astropy was used for the later analysis. As presented in the section 3, we first estimated the flux of the CO(J=7-6) line, and then calculated its luminosity. Using scaling relations from the literature, the luminosity of CO(1-0) was derived. Finally, using an α_{CO} conversion factor appropriate for our source the molecular gas mass of the host galaxy was obtained.

2 Introduction

2.1 Radio Astronomy

2.1.1 Historical Background

Most astronomical objects emit electro-magnetic (EM) radiation which we can detect as light. Not only at optical wavelengths like we are accustomed to seeing in the solar or stellar spectra, but also all the way from gamma and X-rays to the visible domain, perceptible to the eye, up to the radio domain. Radio Astronomy is important because the atmosphere is transparent to radio waves (wavelengths from approximately 1-10mm and above). Together with the optical regime, it is the primary region of the electromagnetic spectrum that is visible from Earth's surface. Away from the obscuring effects of Earth's atmosphere and ionosphere, observations in other regions of the electromagnetic spectrum require high altitude structures or even satellites that fly in orbit.

Radio astronomy has had a major impact on the field of cosmology. Ever since the start of using radio waves to observe astronomical objects, numerous discoveries have been made that changed our view of the universe.

In the 1930s radio astronomy took its first steps when Karl Jansky, an American radio engineer was investigating static interference in transatlantic radio communications. During his research he discovered a mysterious hissing sound originating from a specific direction in the sky. After months of observations and with the assistance of his friend Albert Melvin Skellett Jansky, he realized that this hiss was emanating from the center of our Galaxy, known as the Milky Way. This was the first time radio waves were used for celestial observations. These radio waves are believed to be emitted by ionized particles orbiting around Sagittarius A, the supermassive black hole at the heart of our galaxy. Jansky's pioneering work laid down the foundation for modern day radio astronomy. Hence, the fundamental unit of flux density, the Jansky (Jy), was named after him.

Inspired by Jansky's achievements Grote Reber, an engineer who was 26 years old at that time, took upon himself to construct a remarkable invention. He built the world's first dish antenna radio telescope using materials like galvanized sheet metal, wooden rafters and repurposed spare parts, from a Ford Model T truck. This impressive telescope had a diameter measuring 9.5m. Reber made use of this telescope to create a map of the radio structure within our Galaxy, identify sources of radio waves originating from outside our Galaxy and collect observations that later proved valuable in assisting physicists, with the discovery of non thermal radiation.

2.1.2 Radio Telescopes

Ever since then, multiple radio telescopes were built around the world and they have become a necessary tool for astrophysicists. Modern radio telescope consists of two main parts, the reflecting surface (dish) of the antenna and the feed horn that directs the signal into the receiver. The dish is usually parabolic shaped because it has a single focal point in which incoming light is focused. The dish size determines the telescope's most important capabilities, the sensitivity and the angular resolution. The angular resolution of a telescope is given by Rayleigh's criterion $\theta = 1.22\lambda/D$ where λ is the observed wavelength, D is the diameter of the telescope's aperture and the factor "1.22" is a constant that accounts for the diffraction pattern. There are four types of radio telescopes: the axial (or front feed), the

off-axis (or offset feed), the cassegrain and the gregorian. Firstly, the axial has an antenna at the focal point of the parabolic dish. The cassegrain, uses a secondary convex reflector at the prime focus while gregorian's is concave. In the case of the off-axis only half of the parabola is used.

The response of a telescope's dish optics varies based on the position of the sky relative to where the telescope is pointed. This variation is referred to as the beam pattern, which indicates the pattern in the sky from which signal is being collected and it includes a primary beam (main lobe), which is designed to be the most sensitive region. Its shape is more complex than a straightforward disk because it incorporates the effects of diffraction, the same process that creates Airy disks in optical telescope images. The width of the primary beam is defined as its diameter, and the smaller the diameter, the higher the angular resolution of the observations. There are other areas on the sky where the dish is sensitive, named side lobes, which are concentric circles (if the antenna is round). Even if a bright source is outside the primary beam and in a side lobe, it can still be detected by the telescope. Furthermore, an antenna is termed as high gain antenna if it has a small effective primary beam, as opposed to an antenna with a much wider effective primary beam. Primary beams are, typically, discussed using decibels, a logarithmic scale, because the main lobe's sensitivity is much greater than the side lobes.

When using a parabolic dish, the gain in the direction of the dish's focus is increased while the gain in other directions is reduced, resulting in a beam pattern. An isotropic detector has a gain of one in all directions, while a parabolic dish has a fixed gain value, G isotropic, which is increased in certain directions and decreased in others, limiting the field of view. The center of the beam has a gain relative to the parabola's effective area, which is related to the dish's size and efficiency factor ϵ accounting for reflective surface efficiency and signal loss. The gain also varies with the observing wavelength, with shorter wavelengths having greater gain assuming constant efficiency, although reflective efficiency decreases at higher frequencies. The half-power beamwidth, the size of the primary lobe at the point where the gain decreases by half or three decibels, determines the dish's field of view. The gain is computed by the following formula:

$$G = 4\pi A/\lambda^2 = \epsilon(\pi D/\lambda)^2$$

where λ is the observing wavelength of light, A is the effective area and D the diameter of the dish.

An antenna, such as a half-wave dipole, should be used to transform the incoming light into a voltage. Two dipoles are used to measure two different frequencies, with each polarization being measured by an orthogonal dipole.

The observed light needs to be converted to something measurable, such as voltage. This is accomplished with a series or chain of analogue electronic components, and the antenna is just the beginning of the analogue receiver chain.

Radio telescopes show strong isolation from ambient radiation. The most common types of telescopes and receivers are: antennas (simple dipoles) and paraboloid reflectors, sub-reflectors, or other reflector types. If an observation of a distant source is taken, the typical reflectors used are parabolic. Numerous factors affect a telescope's efficiency such as surface accuracy, pointing, gain e.t.c. A receiver's ability to identify and amplify signals is known as receiver sensitivity which is the weakest possible signal that a receiver will be able to find and process. Noise as well as the collecting area have a critical role on a telescope's sensitivity. The higher the collecting area, the higher the sensitivity.

2.1.3 Radio Interferometry

Because it is not feasible to build extremely large dishes in order to achieve high sensitivity, scientists came up with a revolutionary idea to solve this problem. Using multiple dishes together, working as one. If pointing at the same source simultaneously they all collect the same information with a time delay, because light travels different distance from one dish to the other, that needs to be corrected. This time delay gives positional information about the emitting object. When this delay is corrected then the result is quite similar to the one that a big dish would produce. This technique, known as Radio Interferometry, is the science of combining the signals from various radio telescopes into a single, large synthesis telescope with superior resolving power. The resolution of an interferometric array is given by the relation $\theta = 1.22\lambda/B$ where λ is the observing wavelength and B is the longest possible distance between the dishes that compose the array, which is named baseline. For one pair of antennas there is one baseline, for N antennas there are $N(N-1)$ baselines. For instance, the ALMA 12-meter array switch between its most compressed configuration, with maximum baselines of roughly 150 meters. The array can meet different observational needs thanks to this switching between configurations. There will always be a smallest and a longest baseline between pieces in a given arrangement of dishes. The smallest angular resolution that can be resolved is constrained by the longest baseline while the smallest baseline limits the greatest angular features that can be accurately detected. Interferometers are, in fact, infamous for being unable to accurately measure the total flux of a source. It is advisable to use a single dish that produces a beam larger than the object if one wants to be certain that all the flux from a source has been accurately captured.

Beamforming refers to a type of signal processing that involves summing signals from arrays of receivers with a specific delay from each receiver (to their signals in the same phase) in order to highlight the signal from a specific direction. In general, the positioning of the antennae, along with the Earth's rotation, generates a distinct pattern in the (u,v) plane. The shape and size of the dirty beam on the sky can be determined by performing a Fourier transform on the aforementioned pattern. Convolution of an authentic intensity map of the sky with this dirty beam results in the outcome of the observation session: a dirty image. This dirty image combines actual sky features with artifacts arising from the incomplete coverage of the (u,v) plane.

Another important characteristic is the Field of View (FOV) which is the solid angle indicating the part of the sky the telescope can image at once. The extent of observation for an interferometer is dictated by the dimensions of its constituent antennas and the frequency of observation. FOV is independent of how the antennas are set up within the array. The primary beam, which describes the sensitivity of the antenna regarding angles away from its central axis, is used to quantify the FOV. Primary beam's full width at half-maximum (FWHM), typically, represents the diameter of the FOV. It is crucial to understand that the sensitivity in this field is not uniform; it is highest in the middle and gradually decreases toward the edges. FWHM of the ALMA primary beam is $19''$ when observed at 300 GHz using a 12-meter array, and it measures $33''$ for the 7-meter array. This measurement scales linearly with wavelength, reflecting the individual antenna's diffraction limit, rather than the entire array's.

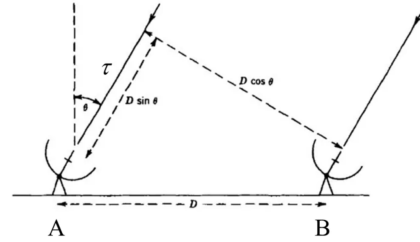
A radio interferometer does not immediately capture an image of the sky. One must use mathematical tools to determine how these measurements relate to the emitting sources in the sky when we use an interferometer to record the amplitude and phase of electromagnetic

waves at a position on the ground. Let's assign names to these two categories of measurements: $I_v(l, m)$: Sky image, the intensity of radio waves in the sky at angular location (l,m), where l and m are measured in radians and ground: Complex visibility $V(u, v)$ of correlated waves measured at position (u,v) on the ground, where u and v are measured in wavelengths. The image $V(u, v)$ that a radio interferometer obtains is the Fourier transform of the sky image $I_v(l, m)$. Fourier theory states that any well behaved signal, including images, can be expressed as the sum of sinusoids. The Fourier transform is a mathematical tool that decomposes a signal into its sinusoidal components. The Van Cittert-Zernike theorem states that there exists a relationship between the mutual spatial coherence function (visibilities) and the sky intensity distribution (image of the sky at a specific frequency). The 2D Fourier relation between the visibility function and the sky signal distribution is:

$$V(u, v) = \iint I_v(l, m) e^{-2i\pi(ul+vm)} dl dm = F\{I_v(l, m)\}$$

$$I_v(l, m) = \iint V(u, v) e^{2i\pi(ul+vm)} du dv$$

The mutual spatial coherence function and the sky intensity distribution are actually Fourier pairs. In aperture synthesis the mutual spatial coherence function, which is a correlation between two points in space, in this case, two radio antennas, is called Visibility. Visibility as a function of baseline coordinates (u,v) is the Fourier transform of the sky brightness distribution as a function of the sky coordinates (l,m). Instead of the absolute position of each point we instead use the spatial difference as shown below.



$$r_2 - r_1 = (x_2 - x_1, y_2 - y_1, z_2 - z_1) = (u, v, w)$$

Each $V(u, v)$ carries information on $I_v(l, m)$ at every point. Visibilities are complex quantities, often expressed as (amplitude, phase). Amplitude, is the Airy function (Bessel function) which gives information about the intensity of the frequency whereas the phase reveals its location.

2.2 AGNs and Quasars

2.2.1 Quasars

As radio astronomy began to develop, it paved the way for groundbreaking discoveries such as pulsars, quasars, radio galaxies, the Cosmic Microwave Background (CMB) just to name a few. In this thesis, the discovery that will be discussed is that of the quasars.

Astrophysicists were baffled by the first observations of quasars. More precisely, they did not really know what was the nature of what they were seeing. In 1960, a radio source named 3C 48, which resembled a star, was identified by Allan Sandage (Lynden-Bell & Schweizer et al. 2010). However, he and other astronomers struggled to identify the absorption lines

in this object's spectrum. Three years later, at the University of Sydney, a new observation technique was utilized by Cyril Hazard in order to locate the radio source 3C 273 with precision (Hazard et al. 2018). Maarten Schmidt from Caltech used the Hale Telescope to examine the spectrum of 3C 273 and found out that the emission lines of this radio source, like those of 3C 48, are at unexpected wavelengths. However, Schmidt infers that he is observing a hydrogen spectrum that has been greatly Doppler shifted. Due to its star-like appearance, 3C 273 is labeled a quasi-stellar object, which will soon be shortened to "quasar".

Throughout the 1960s and 1970s, various hypotheses were suggested to explain quasars, each with its own issues. One theory proposed that quasars were nearby objects, and their redshift was not due to the expansion of space but rather to light escaping a deep gravitational well. However, this would require a massive object, which would also explain their high luminosities (total amount of energy radiated by a celestial object per second). Yet, a star massive enough to produce the measured redshift would be unstable and violate the Hayashi limit. In addition, quasars exhibited forbidden spectral emission lines that were previously only seen in hot gaseous nebulae of low density, making it difficult to explain their power generation and gravitational confinement. The notion of distant quasars also faced serious challenges, such as the implication of energies far exceeding known energy conversion processes, including nuclear fusion. Some proposed that quasars were composed of some unexplored, stable form of antimatter in equally unknown regions of space, which could account for their brightness (Gray et al. 1965). Others speculated that quasars were the white hole end of a wormhole, which was theorized by Albert Einstein, or the result of a chain reaction of numerous supernovae.

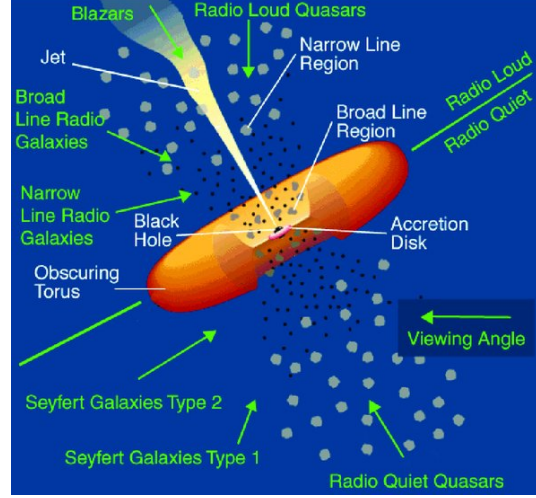
It wasn't until 1970s, when astronomers were persuaded that quasars were indeed distant objects and their spectrum was redshifted due to the expansion of the universe. They also believed that their energy originated from matter in an accretion disc that is being drawn to a supermassive black hole. An accretion disc is formed by diffuse material in orbital motion around a massive central object. Friction, magnetohydrodynamic effects and other forces are responsible for instabilities causing the orbiting gas to spiral inwards to the central body. This process results in heating the gas which leads to radiation. Usually, the central body is a black hole or a star.

Nowadays, we know that quasars are believed to be powered by supermassive black holes (SMBHs) that are located at the centers of galaxies. The intense gravitational forces of these black holes cause gas and dust to be heated to extreme temperatures, which produces prodigious amounts of energy that is emitted as light. Therefore, they are assumed to be some of the most powerful sources of energy in the universe and, thus, some of the brightest objects with luminosities $10^{38} - 10^{42} W$. In other words, they are at least 100 times brighter than our galaxy, the Milky Way, which has approximately a luminosity of $5 \times 10^{36} W$. The luminosity of a quasar is given with the following formula:

$$L_q = \eta \dot{M} c^2$$

where η is the radiative efficiency, which ranges between 0.03-0.4 (Davis & Ari et al. 2011), \dot{M} is the accretion rate of gas onto the SMBH and c the speed of light. Despite the tremendous energy output their size is typically small, around 1pc. Their population evolves with cosmic time with a strong peak at redshifts $z=2-3$.

Yet, quasars are only a subcategory of active galactic nuclei (AGNs). An AGN is a central region of a galaxy with unusually high brightness which completely outshines the rest of the galaxy. The region is dominated by the staggering amount of light emitted by gas and other material as it falls into a SMBH. The masses of SMBHs are normally between $10^6 - 10^{10} M_{\odot}$ (Mickaelian et al. 2015). An AGN emits radiation across the whole electromagnetic spectrum. A galaxy that hosts an AGN is named an Active Galaxy. AGNs can be classified in terms of their radio emission in: radio-loud and radio-quiet. The difference is that jets and lobes contribute to the emission of radio-loud objects, whereas in the radio-quiet the radiation from jets is minimal or non-existent. There are various types of radio-quiet objects such as Seyfert galaxies, Quasi-Stellar Objects (QSOs), Low Ionization Nuclear Emission Line Regions (LINERs). Likewise, radio-loud are separated into quasars, blazars and radio galaxies. Blazars are thought to be quasars whose relativistic jet points exactly towards the observer.



Jets are narrow streams of matter ejected at high velocities from astronomical objects. They are characterized by their collimated nature, which means that they maintain a relatively constant width over long distances. A jet consists of ionized matter which travels almost as fast as light and it is emitted along the rotational axis of the astronomical object. Jets produce synchrotron emission observed at nearly all wavelengths. They are evident in around 10% of quasars, extending from scales of a few pc to Mpc. There are two main types of jets: the galactic jets and the stellar jets. Galactic jets are the ones associated with AGNs. The enormous magnetic fields produced by the spinning SMBH and the surrounding accretion disk are assumed to be the cause of the matter being ejected in these jets.

2.2.2 Hot DOGs

In this thesis, the category of quasars that is studied is that of hot, dust-obscured galaxies (Hot DOGs). They are a rare class of radio quiet quasars and were discovered by WISE in 2010 (Frey et al. 2016). Hot DOGs are extremely luminous with bolometric luminosities $L_{bol} > 10^{13} L_{\odot}$ and are found beyond $z=1$. However, most of their light is obscured by the dense dust around the galactic center. Moreover, they contain large amounts of gas with masses $M_{gas} \approx 10^{10-11} M_{\odot}$. Another noteworthy characteristic is their average temperature $T_{dust} > 60K$ which is considerably higher than that of a typical galaxy. They exhibit prodigious brightness within the infrared segment of the electromagnetic spectrum, but they appear dim or even undetectable in the visible and ultraviolet regions. This unusual property is attributed to the large column density of dust, mentioned above, that surrounds these galaxies, which absorbs the UV and optical light the quasar emits, radiating it back in the infrared as black body emission. Hot DOGs exhibit considerable reddening in the WISE passbands, which is caused by their increased dust content in contrast to ordinary

dust-obscured galaxies. Moreover, they are thought to be in a transition phase between starbursts galaxies and UV-bright quasars (Fan et al. 2018). In this manner, they are great candidates for considering the interaction between SMBHs, star formation, and environment.

The target of this study is a Hot DOG at redshift $z = 4.601 \pm 0.001$. This redshift means that the source is observed around 1.3Gyr after the Big Bang and at a distance of 12.5×10^9 light years (lyrs). Noteworthy is the fact that it is the most luminous dust-obscured quasar known to date. Its bolometric luminosity $L_{bol} = 3.5 \times 10^{14} L_{\odot}$ (Díaz-Santos et al. 2015) and its black hole mass, $M = 4 \times 10^9 M_{\odot}$ imply that the quasar is radiating above the Eddington limit $\lambda = 2.8$ (Tsai et al. 2018). On top of that, observations show that it is part of a multiple-merger with three nearby galaxies. W2246-0526’s spectral energy distribution (SED) is dominated by hot dust with a temperature of $T_{dust} > 450K$.

2.3 Interstellar Medium

2.3.1 Molecular Gas

The interstellar medium (ISM), through its structure and dynamics, is of utmost importance in galaxy evolution. It consists of gas, dust and radiation that occupies the space between stars. On top of that, in its densest regions, known as molecular clouds, lie the birthplace of stars.

Molecular clouds are regions of the ISM where the density and size allow molecules, such as H_2 , to form in contrast to typical regions which contain predominantly ionized gas. There are two main types of molecular clouds: the giant molecular clouds and the small molecular clouds. Giant molecular clouds are normally linked with massive star formation (Bergin & Goldsmith et al. 1996).

Hydrogen (H) and helium (He) make up about 98% of the mass of the ISM, with the remaining 2% being heavier elements like carbon (C), oxygen (O), and other elements astronomers refer to as metals. It is challenging to detect directly molecular hydrogen which is the most abundant molecule in the universe by a factor of 10^4 (Togi & Smith et al. 2016). Hence carbon monoxide (CO), the second most abundant molecule, is commonly utilized as an indicator of the presence of H_2 . The reason for this is that the H_2 molecule does not have a permanent dipole moment, and therefore does not emit EM radiation when it is in the ground state. It is believed that the ratio of CO luminosity to H_2 mass remains relatively constant when averaged over entire galaxies. Inside molecular clouds are regions with higher density named clumps that can lead to star formation in case that gravitational forces are strong enough to cause the gas and dust to collapse.

Sources such as planetary nebulae, stellar winds, and supernovae supply the ISM with matter and energy. The feedback from stars and AGN plays a critical role in regulating how much gas is consumed by star formation in a galaxy and how much is expelled out of it, thus dictating the time in which gas may be completely depleted.

2.3.2 Spectral Lines

When a quantum system (often an atom or molecule) modifies its energy state by changing the arrangement of its electrons, a spectral line is produced. Spectral lines can take two forms: an emission line, which involves the emission of light, or an absorption line, which involves the absorption of light. In the first case, if the system changes to a lower

energy state, the extra energy ΔE will be released as a photon with a frequency given by the Planck's Equation $\Delta E = h\nu$ (where $h = 4.1357 \cdot 10^{-15} \text{eV} \cdot \text{s}$ is the Planck's constant and ν the frequency) creating bright emission over a constrained frequency range. Similarly, if the system shifts to a higher energy state, it will absorb the necessary energy from a photon with the matching frequency, creating a dip or dark patch in the radiation spectrum in the background of this object. The distinct energy levels associated with an atom or molecule are typically unique to a particular species. Consequently, one can employ emission or absorption lines to distinguish and determine the chemical makeup of the material responsible for generating them. In addition, it is feasible to spot any deviation from the line's predicted value since atoms and molecules have distinct, well-known energy states and, consequently, well known frequencies for their spectral lines. This renders it possible for an observer to spot any Doppler shift in a spectral line's frequency brought on by the movement of the substance generating the line with respect to him. Thus, spectral lines offer a beneficial method for comprehending or researching the kinematics of astrophysical objects.

Nevertheless, a natural linewidth is inevitable in all spectral lines. The emitted line will, therefore, have some natural linewidth in frequency space too and it is connected to how likely it is that this transition will occur. There is a lower bound on how precisely one can know the energy and the amount of time it takes for the transition to happen because of the uncertainty principle.

2.3.3 Carbon Monoxide

In this thesis, the spectral line that is used is CO(J=7-6). A molecule like CO is expected to be rotating around its center of mass. CO is comprised of a carbon and an oxygen atom, joined together by a triple covalent bond, making it the most basic form of carbon oxide. When certain molecules exhibit an uneven distribution of electric charges, they create a permanent electric dipole. Due to the uneven distribution of charges, this dipole produces an electric field that is constant. A sinusoidally fluctuating electric field is produced when the molecule rotates at a particular frequency, together with the electric field. This fluctuating electric field will result in electromagnetic radiation according to Larmor's formula. Regrettably, not all molecules have a stable electric dipole such as H_2 which is symmetric. Given that H_2 is the most abundant molecule, this presents a problem. It is crucial to remember that H_2 is produced when two hydrogen atoms combine to form a molecule at high temperatures and densities. It is pivotal to find other tracer molecules that are thought to exist under conditions of similar temperature and density to H_2 . By using a conversion factor, these tracer molecules are then employed to indirectly estimate the amount of H_2 . CO is frequently employed for this purpose.

Indeed, the CO molecule will have rotational kinetic energy. This energy can be determined as half the product of the moment of inertia and the square of its angular velocity.

$$T = \frac{1}{2}I\omega^2 = \frac{1}{2}mr^2\omega^2$$

where T is the kinetic energy, I the moment of inertia, ω the angular velocity, r the distance between the two atoms and m the reduced mass of CO.

$$m = \frac{m_C m_O}{m_C + m_O}$$

The angular momentum (L) is equal to the moment of inertia times the angular velocity $L=I\omega$. Furthermore, the angular momentum can be quantized in accordance with the quantum rule, just like the orbital angular momentum of the hydrogen atom was $L=J\hbar$, where \hbar is the reduced Planck constant $\hbar = h/2\pi$. Thus, the rotational kinetic energy becomes:

$$E_{rot} = \frac{1}{2I}L^2 = \frac{\hbar^2 J(J+1)}{2mr^2}$$

where J is the rotational quantum number. If the environment is really heated, molecules will not survive and will be dissociated. Conversely, in cold environments where low mass molecules can form and survive, the available energy might not be sufficient to excite these molecules to higher energy states. This is due to the fact that low mass molecules have exceedingly high rotational energies, demanding a substantial amount of energy for excitation. Thus, radio emissions in such conditions are presumably produced only by significantly heavier molecules.

3 Data Reduction and Analysis

3.1 Raw Data to Dirty Image

The observations of the CO($J=7-6$) emission line transition of W2246-0526 were conducted using the Band 4 receivers with frequency range 125-163GHz and corresponding wavelength coverage 1.8-2.4mm using the ALMA Observatory. The angular resolution of the observations was 0.35". We used CASA to process and perform a preliminary analysis of the ALMA data. We downloaded the raw data from the ALMA archive and run the script for PI provided with the products in order to obtain the Measurement Set (MS) files. Subsequently, the task *split* was used to create MS files containing only the data from the source, excluding calibration measurements. The seven split files were then concatenated into one concat file with task *concat*, which is used when there are more than one MS files. Thereupon, we subtract the continuum under the line using the *uvcontsub* task in CASA, which performs continuum subtraction in the uv plane. After these steps, everything was ready for cleaning.

Interferometry (visibility) data are converted into images via a procedure named cleaning. The cleaning process was done with *tclean* task, which is based on the CLEAN algorithm, with CASA. *Tclean* creates images from visibility data and reconstructs a sky model. This computational algorithm operates under the assumption that the sky in radio waves is equivalent to a number of point sources within an otherwise empty field of view. It uses an iterative, deconvolution process to identify the positions and strengths of these sources and aims to separate the true signal from the effects of instrumental and atmospheric distortions in the observed data.

CLEAN algorithm is the basis of the majority of deconvolution techniques used in radio interferometry. The position and strength of a putative point source are revealed by the residual image's peak. By subtracting a scaled Point Spread Function (PSF) from the residual image at each point source's position and updating the model, the effects of PSF are removed. The PSF expresses the normalized intensity distribution of a point-source object. Multiple iterations of finding peaks and subtracting PSFs set up the minor cycle.

One of *tclean*'s main parameter is *spw*, which specifies the spectral windows (*spws*) which are going to be cleaned. Every *spw* that includes the required data undergoes the *tclean* operation. Usually, there are four *spws* in each MS file. In the first MS, the *spws* that contain the necessary information are the 16,18,20 and 22 and in the other six MS files there are corresponding *spws* at the same frequencies. Hereafter, when the *spw* 16 is mentioned it means *spw* 16 along with all the *spws* from the other MS files that have the same frequency. The *outframe* parameter defines the spectral frame in which the frequency (or velocity) values will be reported by default and was set to *outframe*='LSRK' (local standard of rest (kinematic) - default). We set the rest-frequency (*restfreq*) as the observed frequency of the line in order to have the cleaned cube already in rest-frame (*restfreq* = 144.02GHz), such that the systemic velocity of the source is at 0km/s. Deconvolver is the algorithm to use in the cleaning process. All of the possible algorithms ('hogbom', 'clark', 'clarkstokes', 'multiscale', 'mtmfs', 'mem', 'asp') follow the Cotton-Schwab CLEAN style of major and minor cycles. Deconvolution algorithm's details are usually contained in the minor cycles and work in the image domain. In our case we use: *deconvolver*='hogbom'. The hogbom algorithm is, essentially, an adapted version of Hogbom Clean. Hogbom CLEAN is best suited for fields of isolated point sources just as in this case. *Specmode* is the image coordinate system(s) and shape(s) and can be set up to form single images (from a single field or from multiple fields producing a mosaic) or multiple fields. The *Specmode*'s cube that was used in our case (because the data is a spectral cube) creates spectral line cubes with one or more channels. The *width* parameter is the channel width of output cube images that is set to 100km/s. *Niter* is the maximum number of iterations before stopping. The stopping criteria determine when to start the next major cycle and when to end the major-minor loop. When *niter* = 1 it creates a dirty image without any cleaning. *Cycleniter*, on the other hand, is the maximum number of minor-cycle iterations before starting a major-cycle and was set to -1. The value of the *threshold* is calculated as $threshold \approx 2.5 \cdot rms$. The rms (Root Mean Square) is found with the *imstat* command (in Jy units) and it varies for each *spw*. Consequently, every *spw* has its own threshold. The average of these thresholds is taken. Furthermore, if the execution of the cleaning process is constrained by a *mask* to where true emission is anticipated to be, CLEAN tends to perform better and is less likely to diverge. This *mask* will apply to all channels if used with a spectral cube. We chose an ellipse as the shape of the *mask* with a large axis of 12'' and a small with 7'', and a position angle of 240°. *Imsize* is the pixel size of the output image. The angular resolution of this observation is $FWHM_{beam} = 8.9''$. We chose *imsize* = 90. Cell parameter is the cell's size which is estimated as: $cell = FWHM_{beam}/10 = 8.9''/10 = 0.89'' \approx 1''$. The key word *weighting* can modify the synthesized beam of the created image and improve the dynamic range. The weighting scheme is therefore critical when constructing a spectral cube. Different weighting schemes can be used to increase the sensitivity of the cube or alternatively increase the angular resolution. The *weighting* parameter has seven possibilities that the user can choose from: 'natural', 'uniform', 'briggs', 'superuniform', 'briggsabs', 'briggsbwtaper' and 'radial'. From these, briggs which allows to optimize angular resolution, noise, and sidelobe levels, is used. The robustness parameter (*robust*) associated to the briggs *weighting* takes values from -2 (close to uniform *weighting*, optimizes angular resolution) to 2 (close to natural, optimizes sensitivity to large angular scales). Robust's scaling is such that R=0 gives a reasonable trade-off between sensitivity and resolution. We chose to image our cubes using two options, 0.5 and 2, to compare between them. *Pbcor* is used to apply pb correction

on the output restored image, to correct for the response of the primary beam.

3.2 Cleaning

We first create the dirty cube (cleaning with $\text{iter}=1$) for every *spw* along with the PSF and PB to find the value for keywords needed to perform the cleaning of the cube, for which we use $\text{niter}=10,000$. After the cleaning is done, we use the CASA viewer to inspect the cubes.

The *spws* 16 and 18 contain the CO(7-6) emission line, while the *spws* 20 and 22 sample the dust continuum emission. Because the emission line lies between the two spectral windows, we decided to clean the two together and image it into a single spectral cube. Likewise, the *spws* 20 and 22 are cleaned together. Because we use two robust values (0.5 and 2), we obtain two cubes for the line and two for the continuum. From now on, only those referring to the line will be used.

3.3 Data Analysis

The first step of the analysis is to export the two cubes that contain the line to FITS (Flexible Image Transport System) image files with the *exportfits* task in CASA. This task produces FITS files with 4 dimensions: Right Ascension (RA), Declination (Dec), radio frequency and polarization. These FITS files are going to be used in the analysis.

Thereupon, Astropy is used in order to open and examine the FITS files. Firstly, the fourth dimension (polarization) is cut and the data are from now on a three-dimensional spectral cube. Then the World Coordinates System (WCS) is applied in the data and the coordinates are transformed from pixel to world. In WCS, Dec is the celestial equivalent of latitude, measured in degrees, while RA is the equivalent of longitude measured in either degrees or hours (15° of RA equal 1 hour).

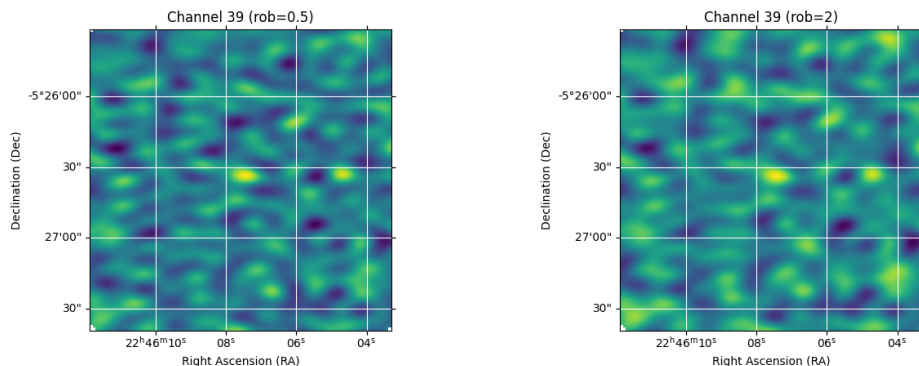


Figure 1: Cleaned images of the source after using the tclean algorithm in the selected channel 39 in WCS, for the two robust values. The source is located at the center of the grid.

In order to extract a spectrum of the source, we define an aperture with a radius $r=7$ pixels, and calculate the flux contained in it for every channel in the cube. Because

the flux is integrated in pixels, we apply a normalization that takes into account the area of the aperture in beam units. We show the spectrum of W2246-0526 for the two datacubes cleaned with different robust parameters in Figure 2.

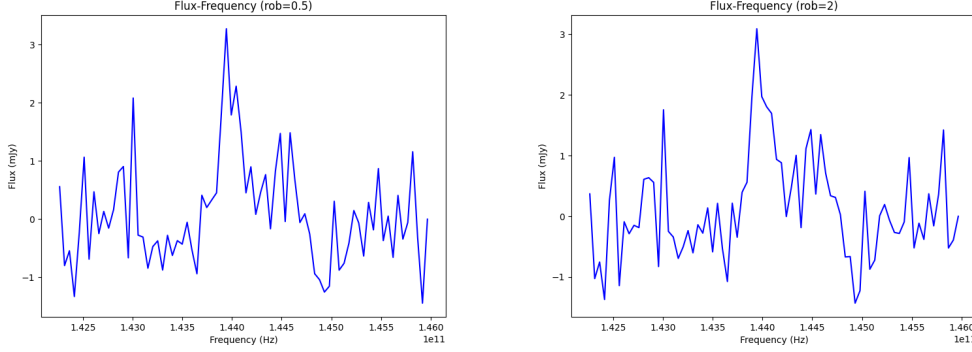


Figure 2: The spectrum of the CO(7-6) emission line for robust=0.5 (left) and for robust=2 (right).

We transform the frequencies of the spectra to velocities using the equation of Doppler shift. First of all, the frequency of CO(7-6) emission at rest frame is known $f_{rest} = 806.6518 GHz$. Therefore, the wavelength of the line at the rest frame is $\lambda_{rest} = c/f_{rest} = 0.3716504 mm$. The wavelength at the observed frame and velocities with doppler effect are computed as follows:

$$\lambda_{obs} = \lambda_{rest} \cdot (z + 1)$$

$$v = \frac{c \cdot (\lambda - \lambda_{obs})}{\lambda_{obs}}$$

where z is the redshift of the source ($z = 4.601$) and λ are the observed wavelengths. With the aim of estimating the total flux of the line, a Gaussian is fit using a maximum likelihood estimation (MLE). This technique is used to specify the parameters of a model. The parameter values are determined in a way that maximizes the likelihood of the observed data being generated by the process described in the model. We will suppose that a Gaussian (normal) distribution can appropriately represent our data. The Gaussian function is given by:

$$G(x) = a \cdot \exp\left(-\frac{1}{2} \frac{(x - \mu)^2}{\sigma^2}\right)$$

where α is the amplitude of the peak, σ is the standard deviation which determines the width of the curve and μ the center of the distribution. MLE finds the parameters α , μ and σ that best fit the data. For initial guesses we use the peak point as the amplitude α and the corresponding ν as the μ . As for the standard deviation, we take data points near the half of the amplitude and calculate their difference in ν axis. This value will be the FWHM estimation and from that the initial guess for σ is computed with the formula $\sigma = FWHM/2.355$. Thus, for robust=0.5 we have these initial values: $\alpha = 3.3 mJy$, $\mu = 158 km/s$ and $\sigma = 348 km/s$. The MLE gives the following optimum values: $\alpha =$

$2.87 \pm 0.70 \text{ mJy}$, $\mu = 94.43 \pm 49.25 \text{ km/s}$ and $\sigma = 164.53 \pm 40.17 \text{ km/s}$. Additionally, for robust=2 we get initial values: $\alpha = 3.1 \text{ mJy}$, $\mu = 158 \text{ km/s}$ and $\sigma = 348 \text{ km/s}$, while the optimum ones are: $\alpha = 3.04 \pm 1.01 \text{ mJy}$, $\mu = 53.58 \pm 47.14 \text{ km/s}$ and $\sigma = 188.75 \pm 40.03 \text{ km/s}$.

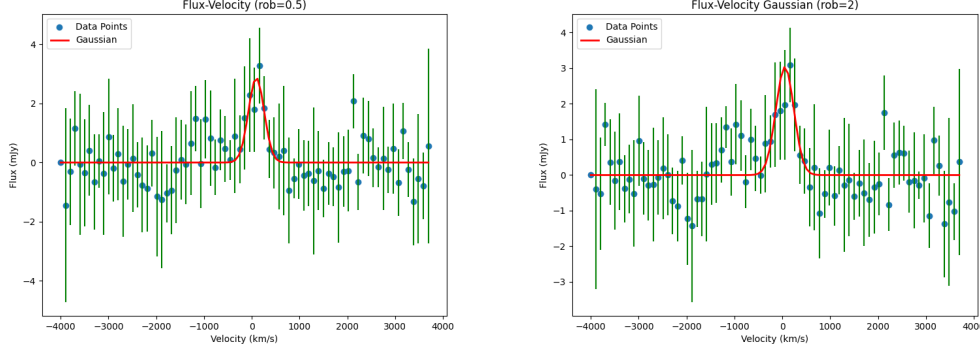


Figure 3: The CO(7-6) spectrum of W2246-0526 for the two robust values with the Gaussian fit and our data points.

We can calculate the flux of the CO(7-6) line as the integral (from -3 sigma to +3 sigma) of this Gaussian. The method we use to calculate the integral is the trapezoidal rule, a versatile method for evaluating the definite integral of a given function. It works by dividing the function's curve into multiple trapezoids and then computing the area underneath it.

In order to calculate the flux's errors, a new aperture is defined away from the source.

$$f_{err}^{channel} = rms \cdot \sqrt{\frac{Aperture}{Beam}}$$

where the aperture is the area of the circular aperture that was used and the rms of each channel was estimated with the median absolute deviation (MAD) method. In statistics, MAD is a reliable indicator of the variability in a univariate sample of a dataset. In the context of calculating the RMS of a circular aperture using the MAD method, it's used to estimate the noise or fluctuations in the aperture's region. The noise level, is indicated by the MAD of the pixel values within the aperture. MAD is defined mathematically, if x_i represents the individual data points and median represents the computed median, as:

$$rms \approx \frac{MAD}{0.67449} = \frac{median(|x_i - median|)}{0.67449}$$

Thus, for robust=0.5: $F_{CO(7-6),rob0.5} = 1.18 \pm 0.44 \text{ Jy} \cdot \text{km/s}$ and for robust=2: $F_{CO(7-6),rob2} = 1.43 \pm 0.39 \text{ Jy} \cdot \text{km/s}$. Total flux's error is:

$$\delta F = \sqrt{\sum_{34}^{45} (f_{err}^{channel} \cdot dv)^2}$$

where channels 33 to 45 are the ones with corresponding values from -3σ to $+3\sigma$, $f_{err}^{channel}$ is the rms times the square root of aperture area in beam units of each channel and dv is

the change in velocity (in km/s) between the channels. In addition, we compute the flux of the line by solving analytically the integral of the Gaussian in the same domain with the following relation:

$$F = a \sqrt{\frac{\pi}{1/2\sigma^2}} = a\sigma\sqrt{2\pi}$$

$$\delta F = \sqrt{(\delta a\sigma\sqrt{2\pi})^2 + (a\delta\sigma\sqrt{2\pi})^2}$$

where δF is the error of the analytic flux, using error propagation. From the above formulas we get $F_{CO(7-6),rob0.5} = 1.18 \pm 0.41 Jy \cdot km/s$ and $F_{CO(7-6),rob2} = 1.44 \pm 0.57 Jy \cdot km/s$. We observe that the values are similar in both methods as expected.

Subsequently, the luminosity of the line is estimated with two separate ways for two different units (Carilli et al. 2013).

$$L = 1.040 \times 10^{-3} F_{CO(7-6)} d_L^2 f_{obs} L_{\odot}$$

$$L' = 3.255 \times 10^7 F_{CO(7-6)} d_L^2 f_{obs}^{-2} (1+z)^{-3} K \cdot km/s \cdot pc^2$$

where $d_L = 42305.530 Mpc$ is the luminosity distance of the source, $f_{obs} = c/\lambda_{obs} = 144.0192476 GHz$ is the observed frequency and L_{\odot} is the solar luminosity. The luminosity distance was measured using a flat ΛCDM cosmology with Hubble's Constant $H_0 = 70 km/s/Mpc$, which represents the current rate of expansion of the Universe, density parameter for matter $\Omega_m = 0.3$ and density parameter for dark energy $\Omega_{\Lambda} = 0.7$ with the relation:

$$d_L = (1+z) \cdot \frac{c}{H_0} \cdot \int_0^z \frac{dz'}{\sqrt{\Omega_m(1+z')^3 + \Omega_{\Lambda}}}$$

Thus, for robust=0.5: $L_{rob0.5} = 3.17 \pm 1.29 \times 10^8 L_{\odot}$ and $L'_{rob0.5} = 1.89 \pm 0.77 \times 10^{10} K \cdot km/s \cdot pc^2$ and for robust=2: $L_{rob2} = 3.85 \pm 2.18 \times 10^8 L_{\odot}$ and $L'_{rob2} = 2.30 \pm 1.30 \times 10^{10} K \cdot km/s \cdot pc^2$. In both cases the errors are found with error propagation method.

$$\delta L = 1.040 \times 10^{-3} F_{CO(7-6)} d_L^2 f_{obs} \delta F L_{\odot}$$

$$\delta L' = 3.255 \times 10^7 F_{CO(7-6)} d_L^2 f_{obs}^{-2} (1+z)^{-3} \delta F K \cdot km/s \cdot pc^2$$

With the aim of estimating the total gas mass, the luminosities of the CO(7-6) line are normalized to CO(1-0) line luminosities as follows:

$$L_{CO(1-0)} = \frac{L_{CO(7-6)}}{r_{71}}$$

$$\delta L_{CO(1-0)} = \sqrt{\left(\frac{\delta L}{r_{71}}\right)^2 + \left(\frac{L \delta r_{71}}{r_{71}^2}\right)^2}$$

where $r_{71} = 0.17 \pm 0.07$. This value is similar to the one used by Decarli et al. (2022) for a sample of quasars at redshifts $z=5-6.7$. Hence, CO(1-0) luminosities of W2246 are $L_{CO(1-0),rob0.5} = 1.87 \pm 1.08 \times 10^9 L_{\odot}$ and $L'_{CO(1-0),rob0.5} = 1.11 \pm 0.64 \times 10^{11} K \cdot km/s \cdot pc^2$ for robust 0.5 and $L_{CO(1-0),rob2} = 2.26 \pm 1.59 \times 10^9 L_{\odot}$ and $L'_{CO(1-0),rob2} = 1.35 \pm 0.95 \times 10^{11} K \cdot km/s \cdot pc^2$ for robust 2.

In order to estimate the total molecular gas mass of W2246 we use the relation (Carilli et al. 2013):

$$M_{H_2} = a_{CO} L_{CO(1-0)}$$

where $a_{CO} = 0.8 \pm 0.1 M_{\odot} (K \cdot km/s \cdot pc^2)^{-1}$ is the conversion factor between CO luminosity and total molecular gas mass (Riechers et al. 2006) and M_{H_2} the molecular gas mass in solar masses $M_{\odot} = 1.98855 \times 10^{30} kg$. Usually, the error for a_{CO} is not reported in the literature so we decided to assume a value of $0.1 M_{\odot}$. The value and the uncertainty in the mass was estimated with a Monte Carlo method. Monte Carlo simulations for propagating uncertainty involve utilizing the uncertainty (Gaussian) distribution for each variable, along with an equation for computing the value needed. By repeatedly choosing random samples from the input variable's specified uncertainty distributions, the desired value, in this case the mass, is determined. The resultant uncertainty distribution of the calculated value is directly derived from the outcomes of these random trials. The mass is computed for every random sample. We get the mean of these values as the mass and the standard deviation as its error.

$$M = \frac{1}{N} \sum_{i=1}^N m_i$$

$$\sigma_M = \sqrt{\frac{1}{N-1} \sum_{i=1}^N (m_i - M)^2}$$

where $N = 100,000,000$ is the number of random samples. The results we get from CO(1-0) line are: $M_{rob0.5} = 8.90 \pm 5.16 \times 10^{10} M_{\odot}$ and $M_{rob2} = 10.8 \pm 7.6 \times 10^{10} M_{\odot}$.

The a_{CO} CO-to-gas mass conversion factor in distant galaxies depends on the type of galaxy, its redshift and its metallicity among other parameters. Currently, dust-to-gas measurements, radiative transfer effects, kinematics and Star-Formation Efficiencies (SFEs), are all thought to influence the value of a_{CO} . Observations point to a Milky Way giant molecular clouds value of $a_{CO} = 4 M_{\odot} (K \cdot km/s \cdot pc^2)^{-1}$ and a value of $a_{CO} = 0.8 M_{\odot} (K \cdot km/s \cdot pc^2)^{-1}$ for Submillimeter Galaxies (SMGs, galaxies observed in submillimeter wavelengths) and quasars, with a possible further increase in low-metallicity galaxies.

We find that our molecular gas mass estimate agrees with the results of Diaz-Santos et al. (2018), who found a value of $M_{CO(2-1)} = 1.5 \pm 0.8 \times 10^{11} M_{\odot}$ based on ALMA observations of the CO(2-1) emission line. In a study conducted by Wang et al. (2010), they obtained a range of molecular gas mass for 8 quasars at redshift $z \approx 6$ of $0.7 \times 10^{10} - 2.5 \times 10^{10} M_{\odot}$. Our result is significantly larger than the range of values obtained in this study. A possible reason for this discrepancy is that the quasars observed in Wang et al. (2010) were selected in the optical, and not in the infrared as Hot DOGs. Also, the redshifts are larger and therefore the host galaxies of these quasars may be in an earlier stage of evolution. In a different study, Lacy et al. (2011), studied two Hot DOGs at redshifts $z = 2.62$ and $z = 2.99$, and they derived molecular gas masses $< 2.8 \times 10^{10} M_{\odot}$ in both galaxies, under the same assumptions for the a_{CO} conversion factor used here. Here again, our measurement is larger than in these two lower redshift Hot DOGs, possibly suggesting the molecular gas content in lower redshift obscured quasars is smaller than the one of slightly higher redshifts.

4 Conclusions

This thesis presents ALMA observations of the CO(7-6) line transition of the Hot DOG W2246 at $z=4.601$. We use the CASA software to clean the data and obtain the emission line cubes. We use Astropy tools to compute the flux of the line and its luminosity. Using a CO brightness temperature ratio of $r_{71} = 0.17 \pm 0.07$ we estimate the luminosity of CO(1-0) line. From this, we derived a molecular gas mass of $M_{H_2} = 10.8 \pm 7.6 \times 10^{10} M_{\odot}$. We compare our results with other studies in the literature and find our estimate of the molecular gas is in agreement with that of Díaz-Santos et al. (2018), who derived a similar value, within the uncertainties, using the CO(2-1) line. However, our estimate disagrees with the studies of Wang et al. (2010) and Lacy et al. (2011) probably due to differences in the quasar sample selection and/or differences in redshift.

References

- Carilli, C. L. "Cool Gas in High-Redshift Galaxies." *Annual Reviews*, 2013.
- Harrison, C. M. "Impact of supermassive black hole growth on star formation." *Nature Astronomy* 1.7 (2017): 0165.
- Hodge, Jacqueline A., and Elisabete da Cunha. "High-redshift star formation in the Atacama large millimetre/submillimetre array era." *Royal Society Open Science* 7.12 (2020): 200556.
- Díaz-Santos, T., et al. "The strikingly uniform, highly turbulent interstellar medium of the most luminous galaxy in the universe." *The Astrophysical Journal Letters* 816.1 (2015): L6.
- Tsai, Chao-Wei, et al. "Super-Eddington accretion in the WISE-selected extremely luminous infrared galaxy W2246-0526." *The Astrophysical Journal* 868.1 (2018): 15.
- Lynden-Bell, Donald, and Francois Schweizer. "Allan R. Sandage, 18 June 1926-13 November 2010." *arXiv preprint arXiv:1111.5646* (2011).
- Hazard, Cyril, et al. "The sequence of events that led to the 1963 publications in nature of 3C 273, the first Quasar and the first extragalactic radio jet." *Publications of the Astronomical Society of Australia* 35 (2018): e006.
- Gray, G. K. "Quasars and Antimatter." *Nature* 206.4980 (1965): 175-175.
- Davis, Shane W., and Ari Laor. "The radiative efficiency of accretion flows in individual active galactic nuclei." *The Astrophysical Journal* 728.2 (2011): 98.
- Mickaelian, Areg M. "AGN Zoo and Classifications of Active Galaxies." *Iranian Journal of Astronomy and Astrophysics* 2.1 (2015): 1-38.
- Frey, Sándor, et al. "Four hot DOGs in the microwave." *Monthly Notices of the Royal Astronomical Society* 455.2 (2016): 2058-2065.
- Fan, Lulu, et al. "The Spectral Energy Distribution of the Hyperluminous, Hot Dust-obscured Galaxy W2246-0526." *The Astrophysical Journal* 854.2 (2018): 157.
- Faerber, Timothy. "Study of CO Emission in Nine Hot Dust-Obscured Galaxies at $z \sim 3$." (2021).
- Bergin, E. A., R. L. Snell, and P. F. Goldsmith. "Density structure in giant molecular cloud cores." *Astrophysical Journal* v. 460, p. 343 460 (1996): 343.
- Togi, Aditya, and J. D. T. Smith. "Lighting the dark molecular gas: H₂ as a direct tracer." *The Astrophysical Journal* 830.1 (2016): 18.
- Bean, Ben, et al. "CASA, Common Astronomy Software Applications for Radio Astronomy." *Publications of the Astronomical Society of the Pacific* 134.1041 (2022): 114501.

- Boogaard, Leindert A., et al. "The ALMA Spectroscopic Survey in the Hubble Ultra Deep Field: CO Excitation and Atomic Carbon in Star-forming Galaxies at $z=1-3$." *The Astrophysical Journal* 902.2 (2020): 109.
- Decarli, Roberto, et al. "Molecular gas in $z \sim 6$ quasar host galaxies." *Astronomy & Astrophysics* 662 (2022): A60.
- Riechers, Dominik A., et al. "CO (1-0) in $z \gtrsim 4$ Quasar host galaxies: no evidence for extended molecular gas reservoirs." *The Astrophysical Journal* 650.2 (2006): 604.
- Díaz-Santos, T., et al. "The multiple merger assembly of a hyperluminous obscured quasar at redshift 4.6." *Science* 362.6418 (2018): 1034-1036.
- Wang, Ran, et al. "Molecular gas in $z \sim 6$ quasar host galaxies." *The Astrophysical Journal* 714.1 (2010): 699.
- Lacy, Mark, et al. "THE STELLAR, MOLECULAR GAS, AND DUST CONTENT OF THE HOST GALAXIES OF TWO $z \sim 2.8$ DUST-OBSCURED QUASARS." *The Astronomical Journal* 142.6 (2011): 196.
- <https://almascience.nrao.edu/>
- <https://casadocs.readthedocs.io/en/stable/>